DE GRUYTER
OPEN

BULGARIAN ACADEMY OF SCIENCES

CYBERNETICS AND INFORMATION TECHNOLOGIES • Volume **16**, No 5
Special Issue on Application of Advanced Computing and Simulation in Information Systems

Sofia • 2016 Print ISSN: 1311-9702; Online ISSN: 1314-4081
DOI: 10.1515/cait-2016-0050

ICA-ASIFT-Based Multi-Temporal Matching of High-Resolution Remote Sensing Urban Images

Fenghua Huang[1,2,3,4,5], *Zhengyuan Mao*[2,3,4], *Wenzao Shi*[2,3,4]

[1]*Postdoctoral Programme of Electronic Science and Technology, Fuzhou University, Fuzhou 350116, China*
[2]*Key Lab of Spatial Data Mining & Information Sharing of Ministry of Education, Fuzhou University, Fuzhou, China*
[3]*National Engineering Research Centre of Geospatial Information Technology, Fuzhou University, Fuzhou, China*
[4]*Spatial Information Engineering Research Centre of Fujian Province, Fuzhou University, Fuzhou, China*
[5]*Yango College, Fuzhou, China*
Emails: fenghuait@sina.com zymao@fzu.edu.cn swz@fjnu.edu.cn

Abstract: *While SIFT* (*Scale Invariant Feature Transform*) *features are used to match High-Resolution* (*HR*) *remote sensing urban images captured at different phases with large scale and view variations, feature points are few and the matching accuracy is low. Although replacing SIFT with fully affine invariant features ASIFT* (*Affine-SIFT*) *can increase the number of feature points, it results in matching inefficiency and a non-uniform distribution of matched feature point pairs. To address these problems, this paper proposes the novel matching method ICA-ASIFT, which matches HR remote sensing urban images captured at different phases by using an Independent Component Analysis algorithm* (*ICA*) *and ASIFT features jointly. First, all possible affine deformations are modeled for the image transform, extracting ASIFT features of remote sensing images captured at different times. The ICA algorithm reduces the dimensionality of ASIFT features and improves matching efficiency of subsequent ASIFT feature point pairs. Next, coarse matching is performed on ASIFT feature point pairs through the algorithms of Nearest Vector Angle Ratio* (*NVAR*), *Direction Difference Analysis* (*DDA*) *and RANdom SAmple Consensus (RANSAC), eliminating apparent mismatches. Then, fine matching is performed on rough matched point pairs using a Neighborhood-based Feature Graph Matching algorithm* (*NFGM*) *to obtain final ASIFT matching point pairs of remote sensing images. Finally, final matching point pairs are used to compute the affine transform matrix. Matching HR remote sensing images captured at different phases is achieved through affine transform. Experiments are used to compare the performance of ICA-ASFIT and three other algorithms* (*i.e., Harris-SIFT, PCA-SIFT, TD-ASIFT*) *on HR remote sensing images captured at different*

times in different regions. Experimental results show that the proposed ICA-ASFIT algorithm effectively matches HR remote sensing urban images and outperforms other algorithms in terms of matching accuracy and efficiency.

Keywords: *Remote sensing image matching, Independent component analysis, SIFT, Affine transform.*

1. Introduction

Matching remote sensing images refers to image processing procedures that match two or more images of the same scenario, captured using different sensors at different phases under different views. It is a key pre-processing step for remote sensing data fusion, variation detection, and object detection [1]. Existing technologies are effective at matching multi-temporal remote sensing images that have small parallax and scale variations. Yet, it still remains a challenge to match multi-temporal remote sensing images that have large parallax and scale variations. In urban areas that consist of many buildings and facilities, solar altitudes and imaging angles of satellite sensors can vary, thus ground objects (e.g., buildings) are prone to rotation, distortion, and drift; shadow distribution is distinctive, key points at different heights are asynchronous, and affine deformation is apparent. Traditional local feature descriptors (e.g., Susan and Brady [2], Harris and Stephen [3], SURF [4], SIFT [5]) are barely robust to affine deformation, so they can only extract fewer feature point pairs from multi-temporal remote sensing images that have large affine deformations, resulting in poor matching accuracy. Although the ASIFT algorithm [6] can extract fully affine invariant features, it generates too many ASIFT feature points, which leads to slow matching speed and a non-uniform distribution of feature point pairs. Traditional matching algorithms (e.g., Harris-SIFT [7-8], PCA-SIFT [9]) have a good matching efficiency, but their matching accuracy is difficult to be guaranteed. Given rough data on exterior orientation elements of oblique images and accurate camera capturing angles, H-SIFT [10], PIF [11], and AIF[12] can match large-inclination aerial images accurately and efficiently. But it is infeasible for remote sensing images to estimate exterior orientation elements and to determine an accurate camera capturing angle. Given the large impact of estimation accuracy on the matching process, these algorithms are unsuitable for matching multi-temporal remote sensing images. To address these problems, this paper proposes a novel matching method, ICA-ASIFT, to match High-Resolution (HR) multi-temporal remote sensing urban images by jointly using Independent Component Analysis (ICA) and ASIFT features to achieve higher matching accuracy and efficiency.

2. ASIFT principles and ICA

2.1. ASIFT principles

SIFT [5] is an invariant-based feature detection algorithm proposed by Lowe in 1999. It is invariant to image scales, rotations, and translations, but it is barely

robust to affine deformations, thus being ineffective at extracting image features in the case of large angle variations. M o r e l and G u o s h e n [6] proposed ASIFT in 2009. Compared to SIFT, which is only invariant to scales, rotations, and translations, ASIFT is also invariant to the two parameters (longitude and latitude angles) that determine the direction of the camera's axis besides that of SIFT, and can achieve affine invariance transformation in a larger scale. This algorithm is suitable for many applications and can match images with large viewing angle variations. Fig. 1 shows the affine camera model [6], where the image u is a planar real object, the small parallelogram at the top right represents where the camera views u, and ϕ and θ represent longitude and latitude angles of the camera's axis, respectively. The third angle ψ is the camera's rotation parameter and λ is a scaling parameter. If the edge of the object is segment-wise smooth, then image distortions caused by viewing angle variation can be locally modelled using an affine plane transform. While capturing the front face of the object, the variation of the axis direction may cause distortion. The basic principle of ASIFT [6] is shown in Fig. 2, where the two squares represent images A and B to be matched and nearby quadrangles represent modelled images.

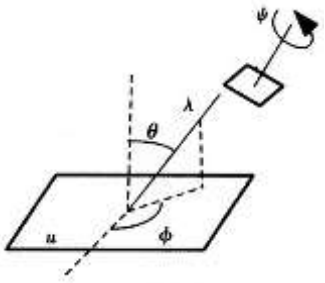

Fig. 1. Model of affine camera

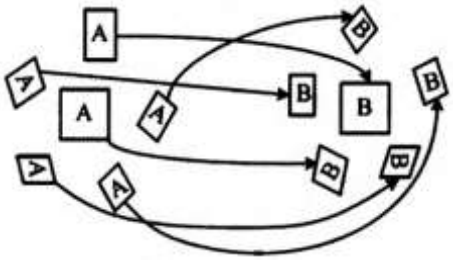

Fig. 2. Principle of ASIFT

In ASIFT, an image transformation is achieved by modelling all possible affine transforms, which are dependent on φ and θ [11]. A certain number of angles φ and θ are sampled, and an affine transform matrix is generated for each sample point to model image direction and inclination variations, that is, to model all viewing angle variation between two images as far as possible. Finally, SIFT matching (128-dimension) is performed on all modelled images using the Nearest Neighbour Distance Ratio method (NNDR) [12]. The ASIFT algorithm that uses NNDR alone is called TraDitional ASFIT (TD-ASIFT) and can match images with large affine deformation more effectively than the original SIFT algorithm, but is slow and barely robust [11]. Owing to the large data of HR remote sensing images, the efficiency and stability of ASIFT-based feature extraction and matching of HR remote sensing images need to be improved.

2.2. Independent component analysis

Independent Component Analysis (ICA) is a method for data processing and signal analysis based on Blind Source Separation (BSS). ICA is usually used to linearly decompose a received signal into statistically independent components [13]. In

ICA, the source signals can be restored from the observed signal using only basic statistical features of the input source signals, without knowing the instantaneous aliasing parameters of the received signals [14]. The fast fixed-point algorithm (FastICA) is a BBS-based feasible variant of ICA proposed by Hyvarinen. Lots of related experiments showed that this algorithm has a desired convergence rate and is thus widely used for feature extraction and dimensionality reduction of high-dimensional data. Principal Component Analysis (PCA) and ICA are two common methods for dimensionality reduction of high-dimensional data. Unlike ICA, PCA assumes that the samples follow a Gaussian distribution and relies only on second-order statistics, based on the covariance matrix to yield excellent performance for large samples. But in ICA, samples are assumed to be mutually independent and higher-order statistics are exploited to ensure that the number of samples has little influence on the results [16]. The PCA constraint is that each component is uncorrelated, while ICA requires components to be strictly independent. The ICA constraint is stronger than that for PCA, resulting in better feature extraction. However, feature extraction in ICA is more complicated than in PCA, especially for large samples. So, ICA is not superior to PCA in terms of operating speed [16, 17].

3. ICA-ASIFT-Based matching of HR remote sensing urban images

The matching process of ICA-ASIFT-Based multi-temporal HR remote sensing urban images is shown in Fig. 3.

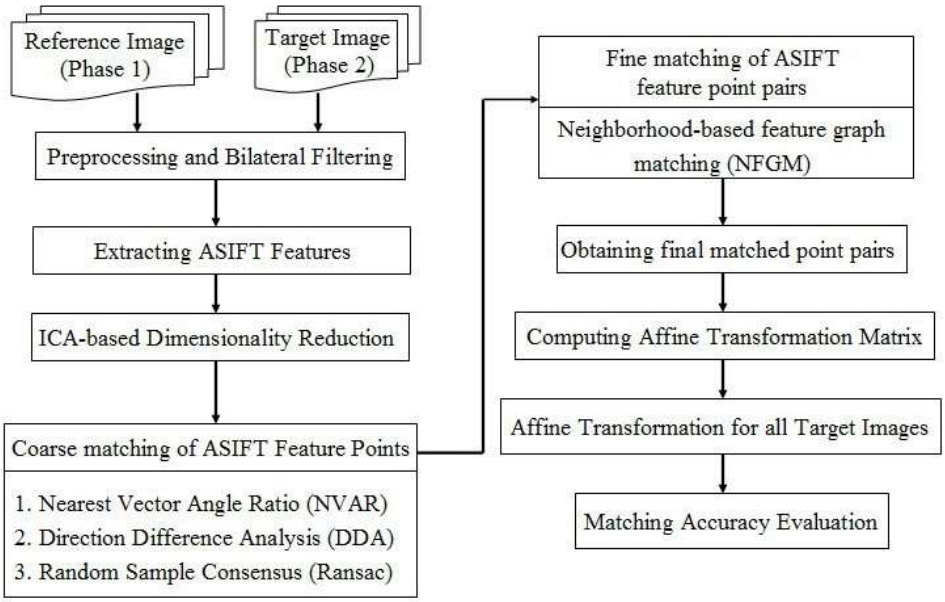

Fig. 3. The matching process of ICA-ASIFT-Based multi-temporal HR remote sensing urban images

3.1. ASIFT-based feature extraction and ICA-based dimensionality

Due to significant noise in the original HR remote sensing images, it is necessary to perform geometrical and radiometric correction, along with smoothing and edge enhancement before feature extraction and matching. A bilateral filter can eliminate noise, while maintaining the edges. It consists of two functions, whose coefficients depend on geometric distance and pixel difference. In this paper, a bilateral filter is used to remove burrs and small holes from images, and to enhance edges of artificial objects in urban regions.

3.2. ASIFT-based feature extraction and ICA-based dimensionality reduction

This paper employs ASIFT to extract features from reference and target images, obtaining the coordinate positions of ASIFT feature points, SIFT feature descriptors (128-dimensional vector), and major directions in each image. The 128-dimensional feature vectors are reduced to 20-dimensional new feature vectors using FastICA.

3.3. Coarse matching of ASIFT feature points

ASIFT feature points are coarsely matched using the Nearest Vector Angle Ratio (NVAR) method, Direction Difference Analysis (DDA) method, and Random Sample Consensus (Ransac) method, respectively.

3.3.1. Two-direction coarse matching of ASIFT feature points based on NVAR

Let A and B be the reference and object images to be matched, N_A and N_B the number of feature points in A and B, and D_A and D_B the set of 20-dimensional feature vector sets of A and B. The angle θ_{ij} between D_A and D_B can be computed as:

(1) $$\theta_{ij}=\arccos(D_A(i)\cdot D_B(j)),\ i=1, ..., N_A,\ j=1, ..., N_B.$$

where θ_i is the set of angles between $D_A(i)$ and all feature vectors in D_B. We sort the N_B values of θ_i in ascending order and compute the ratio of the largest value $\theta_{(i,j_1)}$ to the second largest value $\theta_{(i,j_2)}$, ratio(i) can be computed as:

(2) $$\text{ratio}(i)=\theta_{(i,j_1)}/\theta_{(i,j_2)},\quad j_1, j_2=1, ..., N_B.$$

Let match_{AB} represent the set of matching points in B corresponding to all feature points in A. If ratio(i) is larger than the threshold T_1, then points corresponding to $D_A(i)$ and $D_B(j_1)$ meet the matching condition, that is, $\text{match}_{AB}[i]=j_1$; otherwise, $\text{match}_{AB}[i]=0$. In this paper, threshold T_1 is set to 0.8. In this way, we can obtain the set of matching points in B corresponding to all feature points in A. But many-to-one cases may occur in this matching strategy. Similarly, we can also obtain the set of matching points in A corresponding to all feature points in B, match_{BA}. Many-to-one cases are likely to occur here as well. The intersection of match_{AB} and match_{BA} is computed to eliminate many-to-one or one-to-many cases and obtain the set of coarse matched point pairs set, match_1.

3.3.2. Coarse matching of ASIFT feature points based on DDA

Let A and B be the reference and target images to be matched. Even after coarse matching of ASIFT feature points based on NVAR, there may be mismatches in A and B. Suppose that after NVAR coarse matching, the resulting set match_1 contains the following five point pairs: (A_1, B_1), (A_2, B_2), (A_3, B_3), (A_4, B_4), and (A_5, B_5). The distribution of these pairs is shown in Fig. 4.

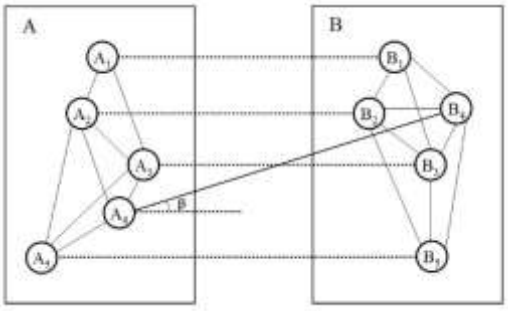

Fig. 4. Distribution of matching points from match1 in A and B

Fig. 4 shows that there is a mismatch in match_1. For example, the slope of the connecting line (A_4, B_4) greatly deviates from the average of other slopes. In this paper, we eliminate abnormal pairs whose direction greatly deviates from the average direction by analyzing the direction difference of pair-wise connecting lines. Let the slope deviation Δf_i be a measure of the direction difference of pair-wise connecting lines, which can be computed as:

$$\Delta f_i = \frac{| f_i - \overline{f} |}{\sqrt{\frac{1}{n_1}\sum_{i=1}^{n_1}(f_i - \overline{f})^2}}, \tag{3}$$

where f_i is the slope of the pair-wise connecting line in match_1 ($f_i=\tan\beta_i$, $i=1,\ldots, n_1$, n_1 is the number of point pairs in match_1; β_i is the angle between the pair-wise connecting line and the X axis) and $\overline{f}$ is the average slope of pair-wise connecting lines.

The feature point pair whose Δf_i exceeds threshold T_2 will be removed, where $T_2=2$ in this paper. As shown in Fig. 4, the slope of the connecting line (A_4, B_4) is larger than the average $\overline{f}$ and $\Delta f_i > T_2$. Thus, it is a mismatch and should be removed. Eliminating mismatches from match_1 yields a set of matched point pairs set, match_2.

3.3.3. Coarse matching of ASIFT feature points based on ransac

Although DDA has the ability to obtain match_2 by removing visually obvious mismatches from match_1, it is ineffective for invisible mismatches. Hence, Ransac is used to address invisible mismatches in match_2, yielding a new set of matched

point pairs set, $match_3$. After this phase, the coarse matching for ASIFT feature points ends.

3.4. Fine matching of ASIFT feature points

Obvious mismatches can be eliminated through coarse matching. But unobvious mismatches need to be removed through fine matching. In this paper, the Neighbourhood-based Feature Graph Matching (NFGM) method is used for fine matching, which further removes mismatches from $match_3$. Each feature point in $match_3$ is regarded as a node in a graph. NFGM determines a mismatch by checking the similarity between neighbourhood topologies of two corresponding nodes in each coarse matched point pair in $match_3$.

Consider that the set $match_3$ contains two matched subsets of points, one from reference images and another from target images. The two subsets have the same number of points. We can construct two feature graphs according to the neighbourhood relationship between feature vectors corresponding to each element of the respective subset: Graph *X* and Graph *Y*, as shown in Fig. 5, where i=1,..., n, j=1,..., n, and n is the number of coarse matched point pairs in $match_3$.

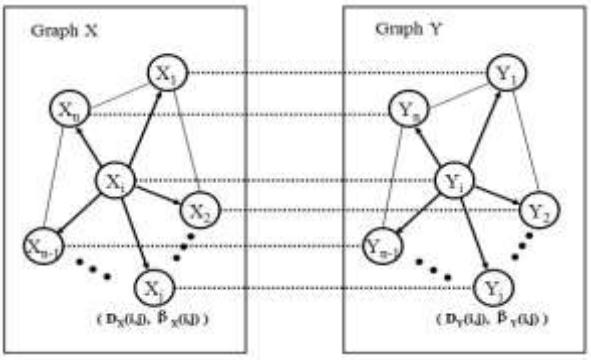

Fig. 5. NFGM-based fine matching of ASIFT feature points

Let matrices $D_X(i, j)$ and $D_Y(i, j)$ denote the length of the directed edges from node i to node j in Graph *X* and Graph *Y* respectively, and their values equal Mahalanobis distance between the vectors of feature points i and j in Graph *X* and Graph *Y* respectively. Let $\beta_X(i, j)$ and $\beta_Y(i, j)$ denote the direction angles of the directed edges from node i to node j in Graph *X* and Graph *Y* respectively, and their values equal the difference between the two direction angles of the ASIFT feature points i and j respectively. Due to the symmetry of these matrices, we only need to compute half their elements, that is, $D_X(i, j)=D_X(j, i)$,$D_Y(i, j)=D_Y(j, i)$, $\beta_X(i, j)=180+\beta_X(j, i)$, and $\beta_Y(i, j)=180+\beta_Y(j, i)$. We normalize D_X, D_Y, β_X, and β_Y and sort elements in each row of these matrices in ascending order, then select the top m ($m<n$) elements in each row of these matrices and yield the new sorted matrices D'_X, D'_Y, β'_X, and β'_Y. In this paper, the neighborhood features of node i in Graph *X* and Graph *Y* can be described effectively by the length vectors ($D'_X(i)$ and $D'_Y(i)$) and the direction angle vectors(β'_X, and β'_Y) of the m edges starting from node i, that is, node i in Graph *X* corresponds to feature vectors $D'_X(i)$ and $\beta'_X(i)$, while node i in *Y*

corresponds to feature vectors $D'_Y(i)$ and $\beta'_Y(i)$. Obviously, the value of m has a great influence on the matching accuracy and efficiency of NFGM, and the optimal value of m, that is threshold T_m, can be obtained by experiments. Related experiments show that NFGM has the best matching accuracy and good matching efficiency when T_m=6, so the optimal value of threshold T_m is 6 in this paper. Finally, we compute distance feature vector difference $\triangle D(i)$ and direction feature vector difference $\triangle\beta(i)$ of node i in X and Y (that is, the i-th coarse matching point pairs in $match_3$), in order to determine whether it is a mismatch. $\triangle D(i)$ and $\triangle\beta(i)$ can be computed as follows, where Dot() is the vector dot product function:

(4) $$\triangle D(i)=\mathrm{Dot}(D'_X(i), D'_Y(i)),$$

(5) $$\triangle\beta(i)=\mathrm{Dot}(\beta'_X(i), \beta'_Y(i)).$$

Obviously, under special condition, if the direction feature vector differences of the i-th node to other nearest m nodes in X and Y are consistent, that is, $\mathrm{Sum}(\beta'_A(i))==0$ and $\mathrm{Sum}(\beta'_B(i))==0$ (where Sum() is a 1D matrix summation function), then the i-th node in X and Y are a match. Generally, mismatches that are left in $match_3$ can be removed by defining thresholds. If $\triangle D(i)>T_3$ and $\triangle\beta(i)>T_4$ (T_3 and T_4 are thresholds), then the i-th node in X and Y are a match. In this paper, thresholds T_3 and T_4 are set to 0.3 and 0.4, respectively. The set of matched point pairs match_final is obtained after fine matching over $match_3$ through NFGM.

3.5. Affine transformation matrix calculation and image matching

We extract ASIFT feature points from reference image A and target image B using the methods discussed in Sections 3.3 and 3.4, and obtain the final set of matched point pairs match_final. The transformation matrix H between A and B is computed based on match_final using the least squares method. The target image is reconstructed through bilinear interpolation (that is, $B=AH$) to achieve the final matching between A and B.

3.6. Evaluation of matching results

Currently, metrics for performance evaluation of digital image matching include the total number of correct matches, uniformity of distribution of correct matches, proportion of correct matches, and matching efficiency. A large number of correct matches and uniform distribution of correct matches implies that matching is effective. The proportion of correct matches refers to the ratio of correct matches to the total number of matches. A high proportion of correct matches mean that matching is accurate. Matching efficiency is the time required of the matching process, also known as time complexity. Small time consumption means that matching is efficient.

4. Experimental results and discussion

4.1. Basic data of the experiment

Our experiment was conducted on WorldView2 images of Shenzhen captured in November 2011 (phase 1) and August 2013 (phase 2). The two images included

three wavebands (RGB) at a resolution of 0.5 m respectively. The former was taken as the reference images (phase 1) and the latter was used as the target images (phase 2). From these two images, we select two typical experimental areas (that is, experimental areas 1 and 2) corresponding to each other, whose size was 1796×1721 and 2280×1824, respectively. WorldView2 images of the two areas captured at different phases are given in Fig. 6, which shows that inside the two areas there was green vegetation, road, bare land, and permanent and temporary buildings. Buildings were distributed in the images unevenly, exhibiting diversity in size, color and distribution. Colors on the roofs of buildings were distinct and edges of buildings were blurred. There were some shadows and walls near the buildings at phase1. Due to the difference in the solar altitude and the imaging angle of the satellite sensors, the images of the two experimental areas captured at different phases both had significant distortions. Especially in the urban districts including dense buildings and artificial facilities, buildings had obvious rotations, distortions, and translations. The distribution of shadows was very distinct, and key points at different heights varied asynchronously, making it difficult to match images using traditional methods.

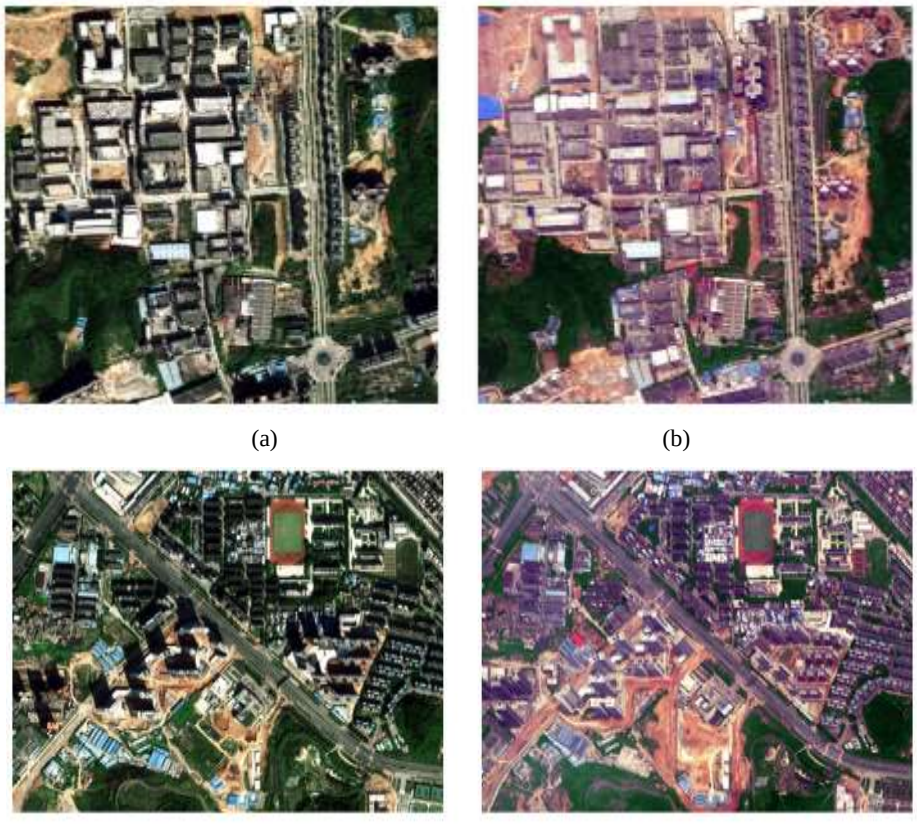

(a) (b)

(c) (d)

Fig. 6. WorldView2 remote sensing images of two experimental areas at different phases: Image of experimental area 1 at phase 1 (a); image of experimental area 2 at phase 1 (b); image of experimental area 1 at phase 2 (c); image of experimental area 2 at phase 2 (d)

4.2. Pre-processing and noise elimination

After obtaining HR WorldView2 images of the two experimental areas, we first pre-process the images through geometrical and radiometric correction. Next, a bilateral filter is used to remove burrs and small holes and enhance edges of artificial objects in urban districts. Here, we take the reference and target images of experimental area 1 as an example to illustrate noise elimination via the bilateral filter. Fig. 7a and c shows corresponding districts (that is, Reg_A and Reg_B) of the reference and target images in experimental area 1 before noise elimination. Fig. 7b and d shows the result images corresponding to Fig. 7a and c after noise elimination using the bilateral filter.

Compared with Fig. 7a and c, buildings and roads in Fig. 7b and d have more distinct edges and the surface of ground objects is smoother. Burrs and small holes in the original images are mostly removed, and walls at the sides of buildings in original images are alleviated. Therefore, the bilateral filter is effective in removing noise from HR images in these experimental areas.

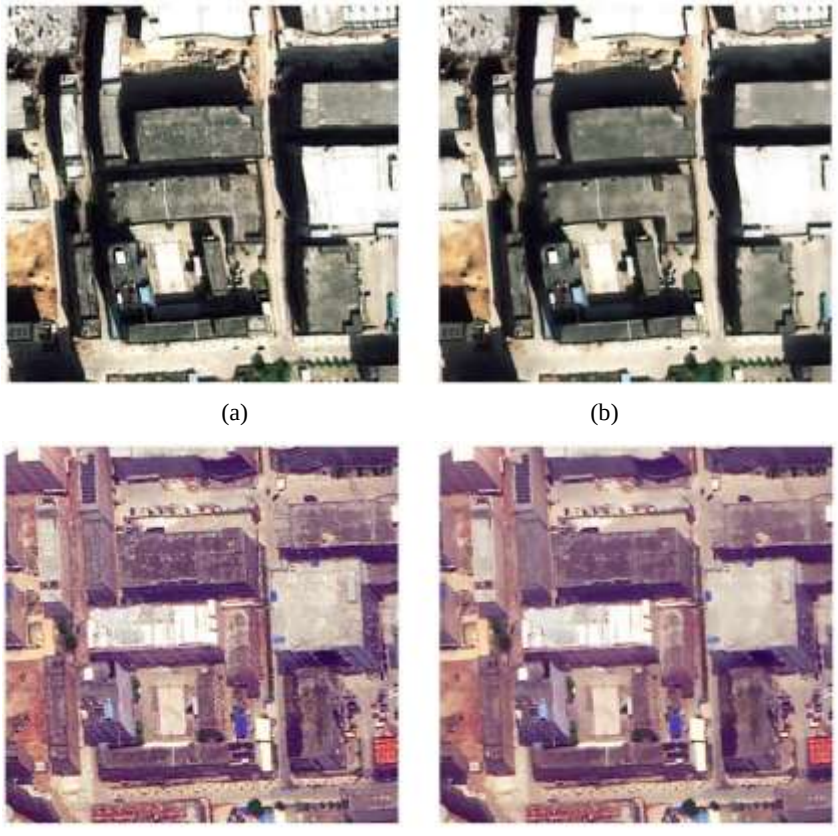

(a) (b)

(c) (d)

Fig. 7. Comparison of the images in parts of experimental area 1 before and after noise elimination: Original image of Reg_A (a); image of Reg_A after noise elimination (b); original image of Reg_B (c); image of Reg_B after noise elimination (d)

4.3. Extraction of ASIFT feature points and dimensionality reduction with ICA

We extract ASIFT features for the reference and target images of the two experimental areas that have been pre-processed and denoised, which yields coordinate positions of the ASIFT feature points, SIFT feature descriptors (128-dimensional vectors), and major directions. To speed up the matching process of subsequent ASIFT feature points, FastICA is used to reduce the dimensionality of SIFT feature vectors from 128 to 20.

4.4. Coarse and fine matching of ASIFT feature points

Coarse matching is conducted on ASIFT feature points by NVAR, DDA, and Ransac sequentially to eliminate mismatches. Fine matching is done via NFGM to obtain the final set of ASIFT matched point pairs for the two images. Fig. 8 shows the distribution and matching of the final set of ASIFT matched point pairs for the reference image (phase 1) and target image (phase 2). In Fig. 8, red and green crosses represent the location of ASIFT feature points for the reference and target images, respectively. Blue lines represent the connecting line for two matching point pairs. From the matching results of two experimental areas in Fig. 8, it can be observed that the proposed ICA-ASIFT provides more correct matches (1920 and 2897 pairs) and the matched point pairs are uniformly distributed, demonstrating the effectiveness of the algorithm.

(a) (b)

Fig. 8. Matched points distribution for reference and target images: Experimental area 1 (1920 matched point pairs) (a); experimental area 2 (2897 matched point pairs) (b)

4.5. Affine transform

Let A_1 and B_1, A_2 and B_2 be the reference and target images for experimental areas 1 and 2 respectively. First, we compute the transformation matrices H_1 and H_2 of the two areas based on the final sets of matched point pairs using the least squares method. Next, target images B_1 and B_2 are reconstructed for the two areas through bilinear interpolation, that is, $B'_1=B_1H_1$ and $B'_2 =B_2H_2$, achieving the final matching of A_1 with B_1 and A_2 with B_2. Image matching of the two experimental areas is shown in Figs 9 and 10.

(a) (b) (c)

Fig. 9. Image matching for experimental area 1: Reference image A1 (a); target image B1 (b); B1 after being matched (c)

(a) (b) (c)

Fig. 10. Image matching for experimental area 2: Reference image A_2 (a); target image B_2 (b); B_2 after being matched (c)

Figs 9 and 10 show that, after the affine transform, the difference between the reference and target images caused by rotation, distortion, or drift is alleviated. Reference images match well with target images for the two experimental areas.

4.6. Comparison and matching performance evaluation

Multi-temporal HR remote sensing images for the two experimental areas are matched using ICA-ASIFT, Harris-SIFT,PCA-SIFT and TD-ASIFT respectively. Matching results are compared each other for performance evaluation. Table 1 shows matching accuracy and efficiency of ICA-ASIFT, Harris-SIFT, PCA-SIFT, and TD-ASIFT. Figs 11 and 12 show the distribution of matching point pairs for multi-temporal HR remote sensing images for the two experimental areas using the four algorithms.

Table 1. Comparison of matching accuracy and efficiency for different algorithms

Experimental area	Matching algorithms	All-matches/mismatches	Proportion of correct matches, %	Matching time, s
Experimental area 1	ICA-ASIFT	1920/104	94.58	272
	Harris-SIFT	433/48	88.91	238
	PCA-SIFT	523/55	89.48	215
	TD-ASIFT	1148/97	91.55	916
Experimental area 2	ICA-ASIFT	2897/181	93.75	281
	Harris-SIFT	501/58	88.42	259
	PCA-SIFT	1221/140	88.53	222
	TD-ASIFT	1229/105	91.46	965

Based on Table 1, Figs 11 and 12, we evaluate the performance of the four algorithms above in terms of total number of matches, distribution of matches, proportion of correct matches, and matching efficiency.

(1) Total number of matches

Table 1 implies that ICA-ASIFT provides the greatest number of matches, followed by TD-ASIFT, while PCA-SIFT and Harris-SIFT lag far behind. This is because compared with SIFT and Harris, ASIFT has the ability to extract more feature points by modelling all viewing angle variations in the two images. But the matching strategy in TD-ASIFT is NNDR, where the ratio between nearest neighbour distance and second nearest neighbour distance cannot be higher than a set threshold (typically 0.36). The matching strategy of TD-ASIFT achieves a high proportion of correct matches, but it removes many correct matches and is unable to eliminate mismatches caused by excessive similarity between textures.

(2) Distribution of matches

Figs 11 and 12 show that matches from ICA-ASIFT are the most evenly distributed, followed by TD-ASIFT. PCA-SIFT and Harris-SIFT provide the least uniformity. This can be explained by the fact that TD-ASIFT uses NNDR as its matching strategy. It removes many correct matches, causing the final matches to be unevenly distributed. Additionally, SIFT is not a fully affine invariant itself, making it difficult to match feature point pairs in urban districts with many buildings that have large inclination and viewing angle variations.

(3) Proportion of correct matches

Table 1 shows that ICA-ASIFT has the highest matching accuracy of 94.58% for experimental area 1 and 93.75% for experimental area 2. TD-ASIFT is ranked second, followed by PCA-SIFT and Harris-SIFT. TD-ASIFT relies on the strict matching strategy of NNDR to eliminate mismatches only once. On the contrary, ICA-ASIFT eliminates mismatches progressively. That is, ICA-ASIFT first performs coarse matching on ASIFT feature points using NVAR, DDA, and Ransac. Next, NFGM is applied for fine matching, further removing mismatches from the coarse matching results. Furthermore, compared with PCA, ICA can maintain original features better, while reducing dimensionality of the 128-dimensional vectors. Commonly, ICA-ASIFT outperforms PCA-SIFT in terms of matching accuracy. Compared with ASIFT, SIFT and Harris are not affine invariant for feature extraction, and Harris is not scale invariant. Hence, while being used to match HR remote sensing urban images captured at different phases with large scale and viewing angle variations, Harris-SIFT provides a high proportion of mismatches and low overall matching accuracy.

(4) Matching efficiency

Table 1 implies that ICA-ASIFT uses slightly more time than PCA-SIFT and Harris-SIFT, but less than 30% of TD-ASIFT running time. For ICA-ASIFT, its number of correct matches is about twice that of TD-ASIFT on average and its matching steps are more than TD-ASIFT. But TD-ASIFT reduces the dimensionality of SIFT features from 128 to 20 through ICA, thus speeding up its matching process over TD-ASIFT.

The analysis above shows that for HR remote sensing urban images captured at different phases, our proposed ICA-ASIFT outperforms TD-ASIFT, PCA-SIFT,

and Harris-SIFT in terms of the number of correct matches, distribution of matches, matching accuracy, and efficiency.

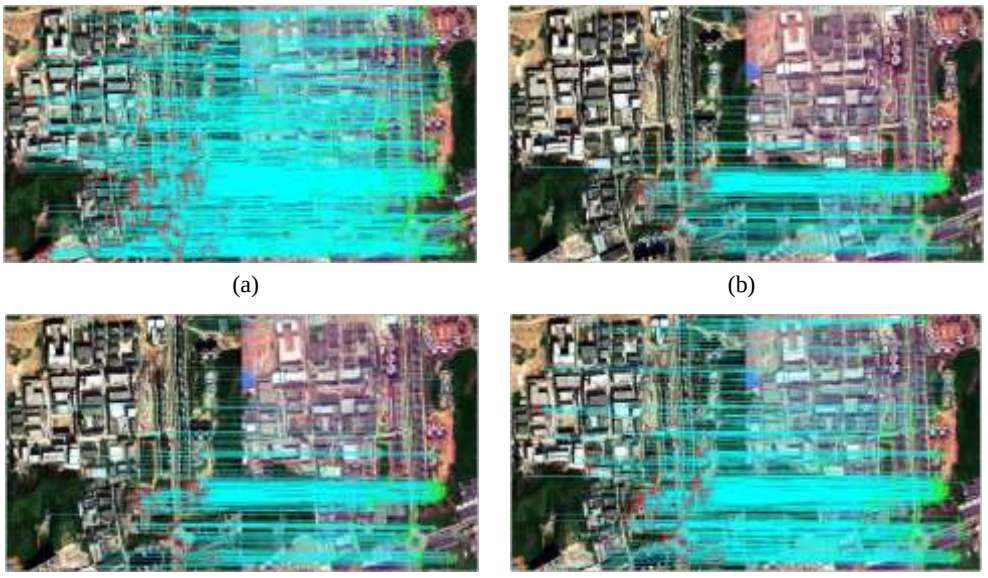

(a) (b)

(c) (d)

Fig. 11. Distribution comparison of matches for images in experimental area 1: ICA-ASIFT (a); Harris-SIFT (b); PCA-SIFT (c); TD-ASIFT (d)

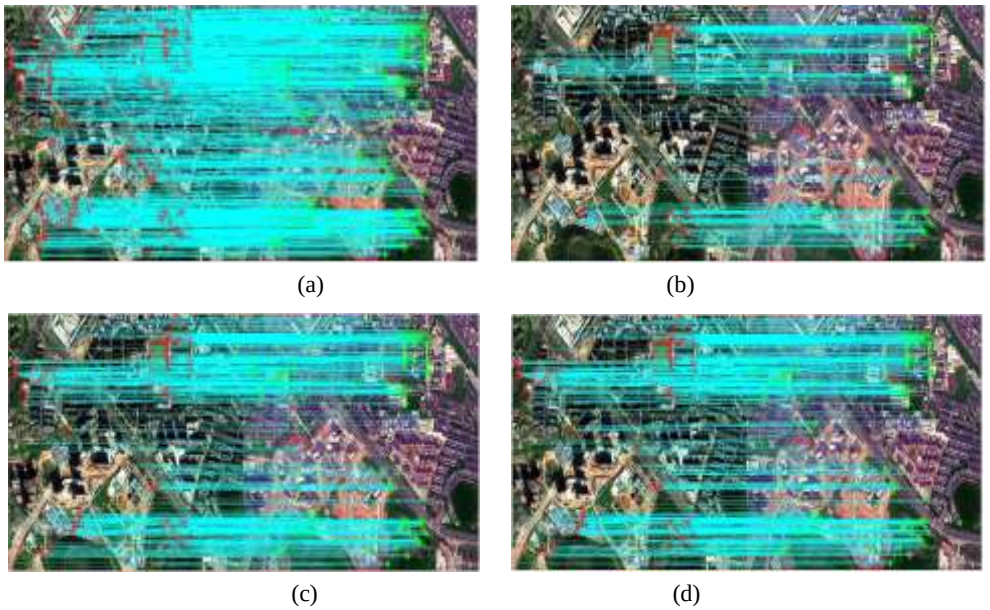

(a) (b)

(c) (d)

Fig. 12. Distribution comparison of matches for images in experimental area 2: ICA-ASIFT (a); Harris-SIFT (b); PCA-SIFT (c); TD-ASIFT (d)

5. Analysis and discussion

Matching multi-temporal HR remote sensing images is a complicated problem that has not yet to be addressed. There may be large differences between reference and target images due to the influence of weather, lighting conditions, shooting angle and time of satellite and camera, sensor type, and uncertainty in remote sensing data. There will be more influences if the research area is enlarged. Thus, a single transformation model alone cannot address this problem. ICA-ASIFT is proposed for affine transform (e.g., inclination, rotation, and viewing angle variation) of multi-temporal HR remote sensing images, and addresses the problem by taking many factors into account. Our proposed ICA-ASIFT has several limitations. First, ICA is used for dimensionality reduction of 128-dimensional features, without further investigation into more effective dimensionality reduction methods. Second, key points are only described with SIFT feature vectors, which are not combined with other features to optimize the selection of features. Finally, a bilateral filter is used to eliminate noise and alleviate the impact of shadows and walls on image matching. Shadows and walls still have a large influence on matching results. We have not found a complete solution to these problems. In future work, we will consider these problems jointly to try to devise a more efficient, accurate, and effective method for matching HR remote sensing urban images captured at different phases.

6. Conclusions

This paper proposes a novel scheme, ICA-ASIFT, for matching HR remote sensing urban images captured at different phases. First, ASIFT and ICA are applied to reference and target images for feature extraction and dimensionality reduction. Next, coarse matching is performed on ASIFT feature points using NVAR, DDA and Ransac. NFGM is used for fine matching to obtain the final set of matches for the two images. Comparison of experimental results shows that our proposed ICA-ASIFT outperforms TD-ASIFT, PCA-SIFT, and Harris-SIFT in terms of the number of correct matches, distribution of matches, matching accuracy, and efficiency.

***Acknowledgments*:** This work was funded by Program for Outstanding Youth Scientific Research Talents Cultivation in Fujian Province University (2015) and China Postdoctoral Science Foundation Project (2015M571963). The authors would like to thank Rui Xu and Qian Weng for useful assistance, suggestions, and discussions.

References

1. Yin, S. W. A Linear Feature-Based Image Rectification Method for HD Remote Sensing Images. – Geomatics Technology and Equipment, Vol. **9**, 2007, No 2, pp. 3-5.
2. Smith, S. M., J. M. Brady. SUSAN-A New Approach to Low Level Image Processing. – International Journal of Computer Vision, Vol. **23**, 1997, No 1, pp. 45-78.

3. H a r r i s, C. J., M. S t e p h e n. A Combined Corner and Edge Detector. – In: Proc. of 4th Alvey Vision Conference, Manchester, United Kingdom, 1988.
4. B a y, H., A. E s s, T. T u y t e l a a r s et al. Speeded-Up Robust Features (SURF). – Computer Vision and Image Understanding, Vol. **110**, 2008, No 3, pp. 346-359.
5. D a v i d, G. L. Distinctive Image Features from Scale-Invariant Key Points. – International Journal of Computer Vision, Vol. **60**, 2004, No 2, 91-110.
6. M o r e l, J. M., Y. G u o s h e n. ASIFT: A New Framework for Fully Affine Invariant Image Comparison. – SIAM Journal on Imaging Sciences, Vol. **2**, 2009, No 2, pp. 438-469.
7. X u, J. J., Y. Z h a n g, H. Z h a n g. Fast Image Registration Algorithm Based on Improved Harris-SIFT Descriptor. – Journal of Electronic Measurement and Instrumentation, 2015, No 1, pp. 48-54.
8. Q i u, J. G., J. G. Z h a n g, K. L i. An Image Matching Method Based on Harris and Sift. – Journal of Test and Measurement Technology, Vol. **23**, 2009, No 3, pp. 271-274.
9. K e, Y., R. S u k t h a n k e r. PCA-SIFT: A More Distinctive Representation for Local Image Descriptors. – In: Proc. of IEEE International Conference on Computer Vision and Pattern Recognition, Washington, 2004.
10. Z h a o, X., Q. Z h u, X. W. X i a o, D. R. L i et al. Automatic Matching Method for Aviation Oblique Images Based on Homography Transformation. – Journal of Computer Applications, Vol. **35**, 2015, No 6, pp. 1720-1725.
11. X i a o, X. G., D. R. L i, B. X. G u o et al. A Rapid Viewpoint Invariant Method for Matching Oblique Images. – Geomatics and Information Science of Wuhan University, Vol. **40**, 2015, No 6, pp. 1-9.
12. X i a o, X. G., B. X. G u o, D. R. L i et al. A Quick and Affine Invariance Matching Method for Oblique Images. – Acta Geodaetica et Cartographica Sinica, Vol. **44**, 2015, No 4, pp. 414-421.
13. Y a n g, H. S., B. H o n g. Principles and Applications of Independent Component Analysis. – Tsinghua University Press, Beijing, 2006.
14. H y v a r i n e n, A., E. O j a. Independent Component Analysis: Algorithms and Applications. – Neural Networks, Vol. **13**, 2000, No 4/5, pp. 411-430.
15. T i c h a v s k y, P. Performance Analysis of the FastICA Algorithm and Cramér-Rao Bounds for Linear Independent Component Analysis. – IEEE Trans, Vol. **54**, 2006, No 4, pp. 1189-1203.
16. R u i, T., C. L. S h e n, Q. T i a n, J. D i n g. Comparison and Analysis on ICA & PCA's Ability in Feature Extraction. – Pattern Recognition and Artificial Intelligence, Vol. **18**, 2005, No 1, pp. 124-128.
17. F e n g, Y., M. Y. H e, J. J. S o n g, J. W e i. ICA-Based Dimensionality Reduction and Compression of Hyperspectral Images. – Journal of Electronics & Information Technology, Vol. **29**, 2007, No 12, pp. 2891-2895.